

Cobalt-Doping Induced Formation of Five-Coordinated Nickel Selenide for Enhanced Ethanol Assisted Overall Water Splitting

Jinchang Xu, Jiaxi Ruan, Yongqi Jian, Jiayu Lao, Zilong Li, Fangyan Xie, Yanshuo Jin, Xiang Yu, Ming-Hsien Lee,* Zhenyou Wang,* Nan Wang,* and Hui Meng

To overcome the low efficiency of overall water splitting, highly effective and stable catalysts are in urgent need, especially for the anode oxygen evolution reaction (OER). In this case, nickel selenides appear as good candidates to catalyze OER and other substitutable anodic reactions due to their high electronic conductivity and easily tunable electronic structure to meet the optimized adsorption ability. Herein, an interesting phase transition from the hexagonal phase of NiSe (H-NiSe) to the rhombohedral phase of NiSe (R-NiSe) induced by the doping of cobalt atoms is reported. The five-coordinated R-NiSe is found to grow adjacent to the six-coordinated H-NiSe, resulting in the formation of the H-NiSe/R-NiSe heterostructure. Further characterizations and calculations prove the reduced splitting energy for R-NiSe and thus the less occupancy in the t_{2g} orbits, which can facilitate the electron transfer process. As a result, the Co₂-NiSe/NF shows a satisfying catalytic performance toward OER, hydrogen evolution reaction, and (hybrid) overall water splitting. This work proves that trace amounts of Co doping can induce the phase transition from H-NiSe to R-NiSe. The formation of less-coordinated species can reduce the t_{2g} occupancy and thus enhance the catalytic performance, which might guide rational material design.

1. Introduction

The oxygen evolution reaction (OER) is now regarded as one of the biggest obstacles to the large-scale application of overall water splitting because of its four-electron mechanism and thus slow kinetics at low overpotential.[1,2] One possible solution is to accelerate the OER process with highly effective OER catalysts.[3] Till now, many highly effective OER catalysts like oxides,[4] sulfides,^[5] selenides,^[6] nitrides,^[7] et al. have been designed to overcome the high overpotential of OER. Another solution is to replace OER with other anode reactions that had faster kinetics. In this case, the ethanol oxidation reaction (EOR) appears as a good alternative for OER because of its lower equilibrium potential and higher value-added resultants.[8,9] Under either circumstance, designing effective bifunctional or trifunctional electrocatalysts to lower the overpotential is of the most importance.

J. Xu, Z. Wang
Guangdong Provincial Key Laboratory of Terahertz Quantum
Electromagnetics
GBA Branch of Aerospace Information Research Institute
Chinese Academy of Sciences
Guangzhou 5 10700, China
E-mail: wangzhenyou@aircas.ac.cn
J. Ruan, Y. Jian, J. Lao, Z. Li, Y. Jin, N. Wang, H. Meng
Guangdong Provincial Key Laboratory of Optical Fiber

J. Ruan, Y. Jian, J. Lao, Z. Li, Y. Jin, N. Wang, H. Meng Guangdong Provincial Key Laboratory of Optical Fiber Sensing and Communications, Siyuan Laboratory, Guangzhou Key Laboratory of Vacuum Coating Technologies and New Energy Materials, Guangdong Provincial Engineering Technology Research Center of Vacuum Coating Technologies and New Energy Materials Department of Physics Jinan University

Guangzhou, Guangdong 510632, China E-mail: nanwang@email.jnu.edu.cn F. Xie
Instrumental Analysis & Research Center
Sun Yat-sen University
Guangzhou, Guangdong 510275, China
X. Yu
Instrumental Analysis & Research Center
Jinan University
Guangzhou, Guangdong 510632, China
M.-H. Lee
Department of Physics
Tamkang University
New Taipei 25137, Taiwan
E-mail: mhslee@mail.tku.edu.tw

(D)

The ORCID identification number(s) for the author(s) of this article can be found under https://doi.org/10.1002/smll.202305905

DOI: 10.1002/smll.202305905

16136829, D. Downloaded from https://oinleibtrary.wilej.co.orn/doi/10.1002/smll.20230959 by National Tawau University, Wiley Online Library on [0512023]. Sethe te Terms and Conditions (https://onlineibtrary.wiley.com/terms-and-conditions) on Wiley Online Library or rules of use; OA articles are governed by the applicable Creative Commons License and Conditions (https://onlineibtrary.wiley.com/terms-and-conditions) on Wiley Online Library or rules of use; OA articles are governed by the applicable Creative Commons License and Conditions (https://onlineibtrary.wiley.com/terms-and-conditions) on Wiley Online Library or rules of use; OA articles are governed by the applicable Creative Commons License and Conditions (https://onlineibtrary.wiley.com/terms-and-conditions) on Wiley Online Library or rules of use; OA articles are governed by the applicable Creative Commons License and Conditions (https://onlineibtrary.wiley.com/terms-and-conditions) on Wiley Online Library or rules of use; OA articles are governed by the applicable Creative Commons License and Conditions (https://onlineibtrary.wiley.com/terms-and-conditions) on Wiley Online Library or rules of use; OA articles are governed by the applicable Creative Commons License and Conditions (https://onlineibtrary.wiley.com/terms-and-conditions) on Wiley Online Library or rules of use; OA articles are governed by the applicable Creative Commons License and Conditions (https://onlineibtrary.wiley.com/terms-and-conditions) on Wiley Online Library or rules of use; OA articles are governed by the applicable Creative Commons License and Conditions (https://onlineibtrary.wiley.com/terms-and-conditions) on Wiley Online Library or rules of use; OA articles are governed by the applicable Creative Commons License and Conditions (https://onlineibtrary.wiley.com/terms-and-conditions) on Wiley Online Library or rules of use; OA articles are governed by the applicable Creative Commons License and Conditions (https://onlineibtrary.wiley.com/terms-and-conditions) on the applicable

www.small-journal.com

Since the catalysis processes contain the adsorption/desorption of several intermediates, the key to improving catalytic performance is to alter the electronic structure so as to optimize the adsorption/desorption capacity for the intermediates^[10,11] yet the mechanism remained unclear.

Transition-metal-based selenides (TMSs) are one of the most promising multifunctional electrocatalysts for future applications. Compared with the benchmark for OER in alkaline media, NiFe LDH,[12,13] the TMSs would show higher electronic conductivity due to the continuity of density of state (DOS) near the Fermi level.^[14] Besides, the crystallographic form of TMSs is abundant, making it convenient to alter the electronic structure to coincide with the reactions by adjusting the crystal structure.^[15] Doping with heteroatoms was also found to be an effective approach to induce phase transition in some TMSs. For instance, Cu(II) would trigger the phase transition from the orthorhombic phase of CoSe₂ to the monoclinic phase of Co₃Se₄.^[16] Coincidently, Zheng et al. found that the doping of P into the cubic phase of CoSe₂ would induce phase transition to the orthorhombic phase of CoSe₂ and thus better adsorption.^[17] Nickel-based selenides are one of the most studied materials for OER and EOR in alkaline media since the nickel sites were found stable and their electronic can be easily altered. [18,19] However, many prior studies pointed out that pure nickel-based materials showed poor catalytic performance for electrocatalysis because of the forbiddance of electron hopping in the $t_{2\sigma}$ orbits.^[10,20,21] In this case, heteroatom/vacancy doping appears as an effective approach to provide additional electron channels and thus could promote the charge transfer process of pure nickel-based materials.^[22-24] In brief, the facile doping-induced phase transition approach is impressive and proved to be effective in altering the electronic structure and thus the catalytic performance of TMSs. However, promoting the OER/EOR catalytic performance of nickel selenides through a facile doping-induced phase transition was seldom re-

Inspired by this, we report a phase transition of nickel selenide induced by a more commonly used atom, cobalt atom. It was observed that trace amounts of cobalt atom doping can induce the phase transition from the hexagonal phase of NiSe (H-NiSe) to the rhombohedral phase (R-NiSe). It appeared as a facile method, both in terms of time and cost, to regulate the electronic structure of nickel selenide through this one-pot hydrothermal method. According to the XRD refinement, up to 18% of H-NiSe can transform into R-NiSe after the doping of Co atoms, resulting in the H-NiSe/R-NiSe heterostructure. Since the Ni atoms in R-NiSe were five-coordinated by Se atoms while six-coordinated in H-NiSe, the reduction in coordination number would lead to more unoccupied states in the $t_{2\sigma}$ orbits. Consequently, additional electron transfer channels would form and thus the catalytic process was facilitated. As a result, the as-prepared Co₂-NiSe/NF showed satisfying catalytic activity toward OER, EOR, and hydrogen evolution reaction (HER), with E_{10} of 1.47, 1.31 and $-0.149~V_{RHE}$, respectively. The Co₂-NiSe/NF also showed favorable stability and can be applied to perform (hybrid) overall water splitting. The density functional theory (DFT) calculations^[25] proved that the superior catalytic performance came from the unique five-coordinated structure of R-NiSe. This work provided an impressive and facile approach to alter the electronic structure and thus the catalytic performance of the materials, which might help rational catalyst design.

2. Results and Discussions

2.1. The Synthesis of Catalysts and Crystalline Phase Characterizations

As shown in Figure 1, the studied selenides were synthesized by an one-step hydrothermal method. First of all, NaBH₄ was used as the reductant to get NaHSe solution so as to prevent the precipitation of Se powder during the next reaction. [26] Meanwhile, a certain amount of cobalt chloride was dissolved into another DMF solution under stirring. Then, after stirring at room temperature for an hour, the two solutions were mixed and reacted at 160 °C for 12 h with a piece of pre-treated nickel foam (NF). By tuning the additive amount of cobalt chloride and Se powder, a series of selenides named Co_v-NiSe_v/NF can be successfully prepared by the simple hydrothermal method.

First of all, in order to get the optimized condition for synthesizing nickel selenide, NiSe_{0.5}/NF, NiSe/NF and NiSe₂/NF (x = 0, y = 0.5, 1 and 2 in Co_x -NiSe_v/NF) were synthesized by altering the additive amount of Se powder. Here, x and y were the relative additive amount of the reactants but not the actual stoichiometric ratio of the materials. As can be seen in Figure S1a (Supporting Information), all the synthesized catalysts showed predominant peaks at 32.4°, 44.0° and 49.7°, which were indexed to (101), (102) and (110) lattice facets of NiSe (JCPDS No. 65-3425). The results indicated the successful synthesis of hexagonal NiSe (H-NiSe). However, if the additive amount of Se powder was insufficient or superfluous, that was NiSe_{0.5} or NiSe₂, the resultants would contain many impurities (Figure S1b, Supporting Information). The impurities might come from the reaction intermediates according to the XRD results. When y = 1, there were no impurities found in the materials. Therefore, the additive amount of Se powder was fixed at y = 1 for further doping experiments.

Then, the additive amount of cobalt chloride was altered to study the interaction of Co atoms and NiSe. As shown in Figure 2a, all the studied materials showed predominant peaks for the hexagonal phase of NiSe (H-NiSe). Additionally, after introducing Co atoms into the lattice, a new set of XRD peaks appeared at 30.5°, 38.5° and 46.2°, which were the characteristic peaks for the rhombohedral phase of NiSe (R-NiSe, JCPDS No. 89–2058). More interestingly, with increasing additive amounts of Co atoms, the characteristic peaks of R-NiSe became more prominent (Figure 2b) while the peaks for H-NiSe remained almost unchanged (for Co_x -NiSe/NF, $0 \le x \le 2$). To be specific, the XRD refinements were conducted as shown in Figure 2b-d. Correspondingly, the peak area of R-NiSe(300) for Co₂-NiSe was more than five times higher than the peak for NiSe (Figure 2c). The result indicated that the introduction of Co atoms might induce partial phase transformation from H-NiSe to R-NiSe. Therefore, the relative peak areas of R-NiSe(300) and H-NiSe(101) derived from the XRD refinements were used to quantify the contents of the two phases of nickel selenides. As shown in Figure 2d, the contents of R-NiSe were 2.4%, 7% and 14.3% in NiSe, Co-NiSe and Co₂-NiSe, respectively. Further increasing the

16136829, 0, Downloaded from https://onlinelibrary.wiley.com/doi/10.1002/smll.202305905 by National Taiwan University, Wiley Online Library on [05/12/2023]. See the Terms and Conditions (https://onlinelibrary.wiley.com

on Wiley Online Library for rules of use; OA articles are governed by the applicable Creative Commons License

www.small-journal.com



Figure 1. The schematic diagram of the synthesis process.

additive amount of Co wouldn't continue to increase the relative content of R-NiSe, as shown in Figure S2 (Supporting Information). According to the XRD refinement, the R-NiSe content in $\text{Co}_4\text{-NiSe/NF}$ was 18%, slightly higher than that of $\text{Co}_2\text{-NiSe/NF}$ (Figure S2c, Supporting Information). For $\text{Co}_8\text{-NiSe/NF}$ and $\text{Co}_{16}\text{-NiSe/NF}$, only H-NiSe would form even with higher Co doping amounts. Further, for $\text{Co}_{32}\text{-NiSe/NF}$ and $\text{Co}_{64}\text{-NiSe/NF}$, even the XRD peaks for H-NiSe disappeared (Figure S2a,b, Supporting Information). In summary, only the moderate addition of Co would lead to the formation of R-NiSe. Without the addition of Co, almost all (\approx 98%) of the NiSe was in the phase of hexago-

nal. For x = 1, 2 and 4, the relative contents of rhombohedral phase were 7%, 14.3% and 18%, respectively. Further increasing the additive amount of Co up to x>4 would not induce the phase transition.

Moreover, the XRD peak for R-NiSe(300) shifted to a lower angle as can be seen in Figure 2b, indicating an expansion of the R-NiSe lattice. The lattice facet distance of R-NiSe(300) was 2.903 Å for NiSe while 2.915 Å for Co_2 -NiSe, which meant a $\approx 0.4\%$ of tensile strain was found in the formative R-NiSe in Co_2 -NiSe (Figure S2e, Supporting Information). Meanwhile, the lattice facet of H-NiSe(101) remained almost unchanged for the

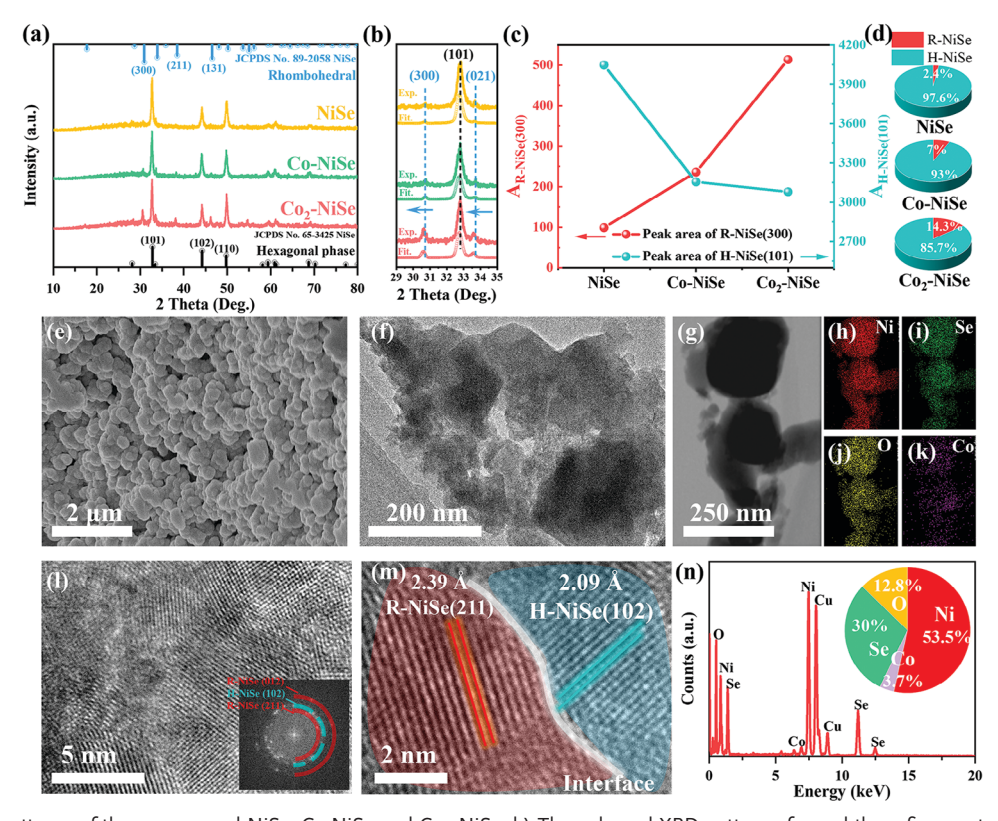


Figure 2. a) XRD patterns of the as-prepared NiSe, Co-NiSe and Co₂-NiSe. b) The enlarged XRD pattern of a and the refinement results. c) The XRD peak area of hexagonal-NiSe (101) and rhombohedral-NiSe (300) for different samples. d) Pie charts of the crystalline phase components in NiSe, Co-NiSe and Co₂-NiSe, respectively. e) SEM image of Co₂-NiSe/NF. f) TEM image of Co₂-NiSe/NF. g-k) STEM and corresponding element distributions of Co₂-NiSe/NF. l,m) HRTEM images of Co₂-NiSe/NF. The inset is the FFT image of (l). n) The element contents of Co₂-NiSe/NF characterized by STEM.

www.advancedsciencenews.com

SMQI

www.small-journal.com

three catalysts, with only ≈0.1% of tensile strain found from the XRD results. The considerable tensile strain for R-NiSe(300) might cause by two reasons. First, the R-NiSe and H-NiSe showed lattice mismatch. In the H-NiSe lattice, the Ni atoms were sixcoordinated by Se atoms in a P63/mmc space group (Figure S3, Supporting Information). While in the R-NiSe lattice, the Ni atoms were five-coordinated by Se atoms in an R3m space group (Figure S4, Supporting Information). The lattice mismatch of the two phases would lead to considerable strain, especially for the minority phase. That's why R-NiSe showed more obvious tensile strain than H-NiSe. The other reason for the tensile strain was the formation of vacancies.^[27] The introduction of Co atoms would lead to phase transformation and thus lattice mismatch, which would inevitably introduce vacancies into the lattice. Therefore, both H-NiSe and R-NiSe lattices showed tensile strain with the existence of vacancies.

The morphology of the as-prepared selenides was studied by scanning electron microscopy (SEM) and transmission electron microscopy (TEM). The low-magnification SEM images (Figures S5-S9, Supporting Information) indicated that the surfaces of nickel foams were fully covered by the desired selenides. For NiSe/NF, the sample showed generally nanosheet morphology according to the SEM results (Figure S6, Supporting Information). While after doping with Co atoms, the morphology changed a lot, especially for Co₂-NiSe/NF (Figure 2e; Figure S9, Supporting Information). Generally, the Co₂-NiSe/NF showed coral-like morphology. Both the nanosheet and coral-like morphology would help expose a larger surface area and prevent agglomeration in the self-standing electrode.[28] The difference in morphology was supposed to originate from the different lattices. For Co₀-NiSe/NF, it composed of over 98% of H-NiSe, and thus the lattice arrangement was more likely to be in a good order. Consequently, the morphology of Coo-NiSe/NF was more regular. Instead, the Co₂-NiSe/NF was composed of \approx 14% of R-NiSe and 86% of H-NiSe. The crystalline mismatch of the two phases would bring more chaos in the lattice and thus the overall morphology of Co₂-NiSe/NF was more disordered. As a result, the formative morphology changed after the Co induced phase transition process.

Further, according to the TEM results, the coral-like structure in Co₂-NiSe/NF consisted of many polycrystalline particles (Figure 2f,g) and the particle size was around several hundred nanometers. Additionally, the element distribution spectrum (EDS) from STEM confirmed that Ni, Se, O and Co were distributed uniformly in Co₂-NiSe/NF (Figure 2h,i).

Then, the polycrystal nature of Co₂-NiSe/NF was studied by high-resolution TEM (HRTEM). In Figure 2l, clear lattice fringes can be seen, indicating good crystallinity of Co₂-NiSe/NF. The fast Fourier transform (FFT) inserted in Figure 2l revealed the coexistence of R-NiSe(012), R-NiSe(211) and H-NiSe(102) lattice facets. There was also a heterostructure interface for R-NiSe(211) and H-NiSe(102) found in Figure 2m. The result indicated that the two phases of NiSe grow adjacent to each other, which might have a strong electron exchange and might benefit the electrocatalysis process. Besides, the EDS result in Figure 2n confirmed the existence of Co atoms in the lattice, with a content of 3.7% in the studied elements. Considering that there were no XRD peaks for cobalt selenide species, the Co atoms might exist in the NiSe lattice as a dopant.

2.2. The Chemical State of the Catalysts

The chemical states of Ni, Se and Co in the materials were then studied by X-ray photoelectron spectroscopy (XPS). The XPS survey spectrums are shown in Figure S10 (Supporting Information) and predominant peaks for Ni, O, C and Se can be seen from the survey spectrum. Moreover, peaks were observed at $\approx\!187$ eV in the XPS survey spectrum for all the samples, which might be attributed to B 1s or Se LMM. The B element might come from the superfluous NaBH $_4$ during the synthesis process. Besides, the corresponding peak tables derived from the survey spectrum can be found in Tables S1–S5 (Supporting Information). According to the table, the contents of Co atoms in both Co-NiSe and Co $_2$ -NiSe were less than 1 atom.%, consistent with the EDS results.

The high-resolution Ni 2p XPS patterns for NiSe, Co-NiSe and Co₂-NiSe are shown in Figure 3a. The peak was then further deconvoluted to study the chemical state. According to previous literature, $^{[7,29]}$ peaks at \approx 853 and 870.5 eV were the characteristic peaks for Ni^0 $2p_{3/2}$ and Ni^0 $2p_{1/2}$. Then, peaks at ≈ 855.4 and 872.9 eV were indexed to Ni²⁺ $2p_{3/2}$ and Ni²⁺ $2p_{1/2}$, respectively. Peaks at \approx 856.9 and 874.4 eV were ascribed to Ni³⁺ 2p_{3/2} and Ni³⁺ $2p_{1/2}$. Generally, the Ni 2p peaks showed a positive shift after the doping of Co atoms, indicating a decrease in electron density near the Ni atoms. The deconvolution results also showed the increasing content of high valent-state Ni species after Co doping. The above results proved that the Co dopant would have strong electron interaction with Ni atoms and can alter the chemical state of Ni by adjusting the doping amount. Similarly, the Se 3d XPS patterns also showed a positive shift after the doping of Co atoms (Figure 3b). The deconvoluted peaks at ≈53.8, 54.5 and 58.7 eV were ascribed to Se²⁻, Se⁰ and Se^{δ +}, respectively. [30]

Generally, as shown in Figure 3c, the contents of both high valent-state Ni and Se species increased after the introduction of Co atoms to the lattice. Interestingly, the O atoms also showed electron deficiency according to the O 1s XPS results (Figure S11, Supporting Information). The decrease in electron density near Ni, Se and O was then proved to be caused by the electron transfer to Co atoms (Figure S12, Supporting Information). In the American National Institute of Standards and Technology (NIST) database for XPS, the lowest binding energy for Co $2p_{3/2}$ is 777.8 eV for Co 0 $2p_{3/2}$. However, in our work, the peak for Co $2p_{3/2}$ centered at \approx 775 eV (dash line in Figure S12, Supporting Information). The result indicated a great increase in electron density near Co atoms.

Raman spectrum was conducted to study the molecular vibration of the materials. As shown in Figure 3d, the as-prepared NiSe/NF showed only one vibration peak in the studied region. The peak at $\approx\!250~\text{cm}^{-1}$ for both NiSe/NF and Co₂-NiSe/NF was ascribed to T_g mode of Se-Se in NiSe. $^{[32]}$ After doping with Co atoms, many vibration modes appeared in the low wavenumber region. For Co₂-NiSe/NF, peaks at $\approx\!170$ and 230 cm $^{-1}$ were ascribed to the bending and stretching mode of Se-Se in the disordered CoSe. $^{[33]}$ The peak at 211 cm $^{-1}$ was the A_g mode of Co-Se. On the one hand, the existence of CoSe vibration modes in the Raman spectrum again proved the successful introduction of Co atoms into the NiSe lattice. On the other hand, the introduction of Co atoms would increase the degree of disorder in the NiSe lattice, which was proven by the existence of disordered Se–Se mode.

16136829, 0, Downloaded from https://onlinelibrary.wiley.com/doi/10.1002/smll.202305905 by National Taiwan University, Wiley Online Library on [05/12/2023]. See the Terms

conditions) on Wiley Online Library for rules of use; OA articles are governed by the applicable Creative Commons License

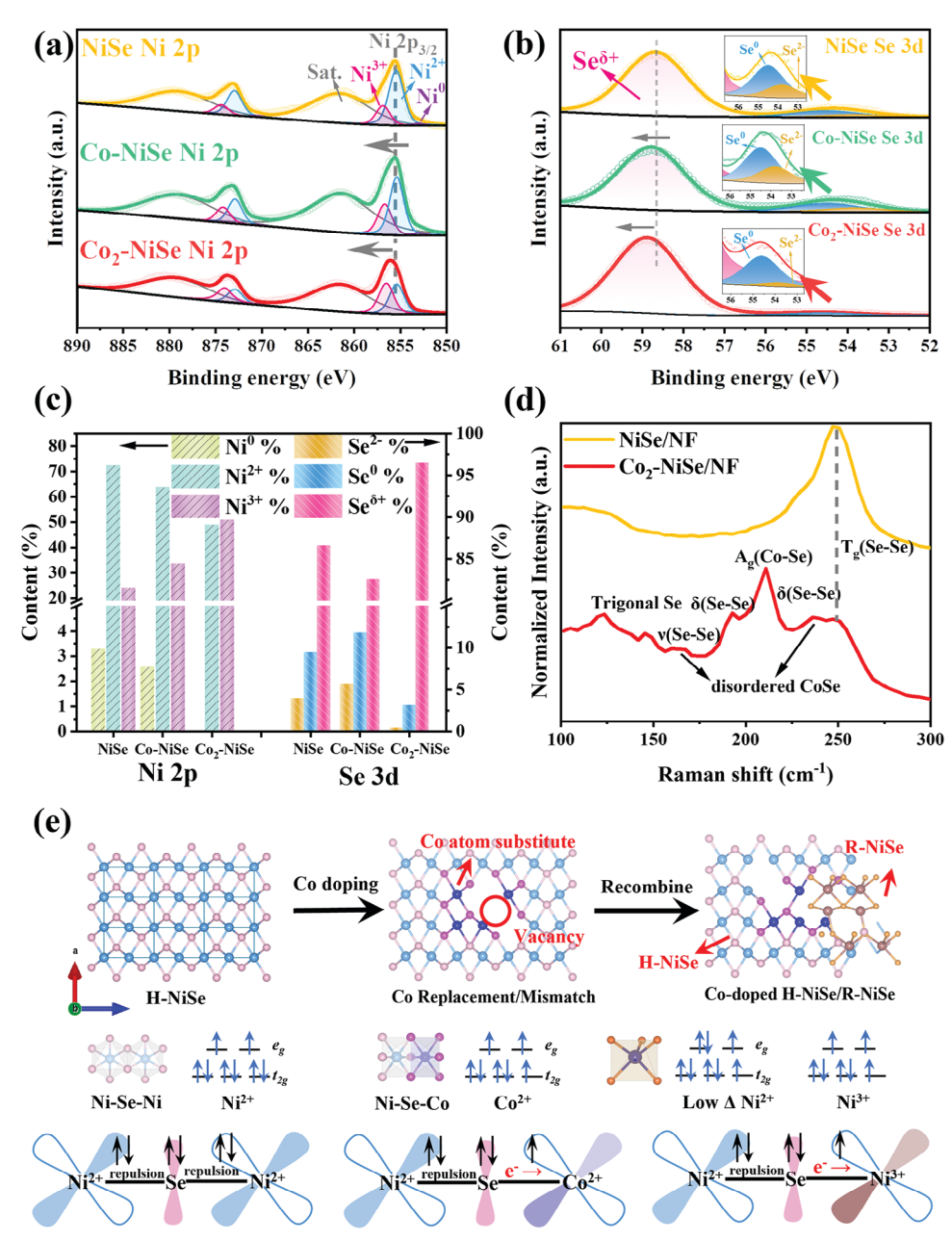


Figure 3. The high-resolution XPS patterns of a) Ni 2p and b) Se 3d for NiSe, Co-NiSe and Co₂-NiSe, respectively, c) Relative contents of Ni and Se in different valent states for the studied samples according to the deconvolution of high-resolution XPS results. d) The Raman spectrum of NiSe/NF and Co₂-NiSe/NF. e) The schematic diagram of the electron transfer process in the lattice.

In summary, the XPS results proved that the doped Co atoms showed strong electron interaction with the NiSe lattice, causing electron transfer from Ni, Se and O to Co atoms. The Raman spectrum indicated the successful introduction of Co into NiSe lattice, and the introduction of Co atoms would inevitably bring chaos and thus vacancies to the lattice.

According to the above results, a clear picture can be drawn to describe the electron transfer in the studied materials (Figure 3e). First of all, it has been widely reported that electrons can transfer from the d orbits of metal atoms to the p orbits of O or Se atoms through unoccupied states in t_{2g} orbits.^[34] The t_{2g} orbits of Ni²⁺ were fully occupied as illustrated in Figure 3e. Therefore, the electron transfer between Ni²⁺ and the adjacent O or Se atoms is widely reported to be non-ideal.[35] For H-NiSe, the valent state of Ni was relatively low, with over 70% of Ni²⁺ according to the XPS results. Under this circumstance, the electron transfer between Ni and the neighboring Se/O atoms was poor (Figure 3e, left). However, if doping with Co atoms, even didn't induce phase $\,$ transformation, the unoccupied state in Co^{2+} - t_{2g} would help better electron transfer (Figure 3e, middle). Further, in our work, the doping of Co atoms would induce partial phase transformation, leading to a Co-doped H-NiSe/R-NiSe structure with over 50%

16136829, D. Downloaded from https://oinleibtrary.wilej.co.orn/doi/10.1002/smll.20230959 by National Tawau University, Wiley Online Library on [0512023]. Sethe te Terms and Conditions (https://onlineibtrary.wiley.com/terms-and-conditions) on Wiley Online Library or rules of use; OA articles are governed by the applicable Creative Commons License and Conditions (https://onlineibtrary.wiley.com/terms-and-conditions) on Wiley Online Library or rules of use; OA articles are governed by the applicable Creative Commons License and Conditions (https://onlineibtrary.wiley.com/terms-and-conditions) on Wiley Online Library or rules of use; OA articles are governed by the applicable Creative Commons License and Conditions (https://onlineibtrary.wiley.com/terms-and-conditions) on Wiley Online Library or rules of use; OA articles are governed by the applicable Creative Commons License and Conditions (https://onlineibtrary.wiley.com/terms-and-conditions) on Wiley Online Library or rules of use; OA articles are governed by the applicable Creative Commons License and Conditions (https://onlineibtrary.wiley.com/terms-and-conditions) on Wiley Online Library or rules of use; OA articles are governed by the applicable Creative Commons License and Conditions (https://onlineibtrary.wiley.com/terms-and-conditions) on Wiley Online Library or rules of use; OA articles are governed by the applicable Creative Commons License and Conditions (https://onlineibtrary.wiley.com/terms-and-conditions) on Wiley Online Library or rules of use; OA articles are governed by the applicable Creative Commons License and Conditions (https://onlineibtrary.wiley.com/terms-and-conditions) on Wiley Online Library or rules of use; OA articles are governed by the applicable Creative Commons License and Conditions (https://onlineibtrary.wiley.com/terms-and-conditions) on Wiley Online Library or rules of use; OA articles are governed by the applicable Creative Commons License and Conditions (https://onlineibtrary.wiley.com/terms-and-conditions) on the applicable

www.small-journal.com

of Ni³⁺ (Figure 3e, right). In the lattice of R-NiSe, the Ni atoms were five-coordinated by Se atoms while six-coordinated in H-NiSe. In other words, the coordination number of Ni in R-NiSe was smaller than that of H-NiSe, which would weaken the intensity of the crystal field and lead to lower splitting energy (Δ). Therefore, the electrons are more likely to occupy the e_g orbits in R-NiSe, leaving an unoccupied state in the t_{2g} orbit. Further discussions can be seen in the DFT calculations section below. Similarly, the Ni³⁺ with 3d⁷ configuration would leave an unoccupied state in t_{2g} as Co²⁺. Therefore, the electron transfer in Co₂-NiSe/NF was expected to be much better than that of NiSe/NF, which might bring better catalytic performance.

2.3. The Catalytic Performance Toward OER in Alkaline Media

The catalytic performance of the as-prepared catalysts for OER was studied in 1.0 M KOH aqueous solution. Cyclic voltammetry (CV) experiments at a scan rate of 5 mV s⁻¹ were first conducted to study the redox properties of the materials and get stable data. As shown in Figure S13 (Supporting Information), all the studied materials showed broad redox peaks at 1.2–1.5 $V_{\rm RHE}$, which were ascribed to the redox of Se or Ni species. [36,37] Therefore, the scan rates were reduced to 1 mV s⁻¹ and the positive-sweep round of the CVs was used as polarization curves to study the catalytic performance. As shown in **Figure 4a**, all the synthesized catalysts showed benign catalytic performance toward OER. Among them, Co₂-NiSe/NF and Co₄-NiSe/NF showed the best catalytic activity, with an overpotential of only 240 mV to reach the current density of 10 mA cm⁻². The catalytic performance also outperformed many recently reported electrocatalysts toward OER (Table S6, Supporting Information). Accordingly, the η_{10} for NiSe/NF was 270 mV. There was a 30 mV of promotion after doping with Co atoms and the formation of R-NiSe according to the polarization curves.

The Tafel plot was shown in Figure 4b and the corresponding Tafel slopes were calculated as shown in Table S7 (Supporting Information). According to the results, the Tafel plots can be generally divided into three regions: the non-Faradic region, the self-redox region, and the OER region as can be seen in Figure S14 (Supporting Information). The OER kinetics was studied in the OER region with a higher overpotential. Interestingly, the Tafel slope decreased after the doping of Co atoms [38] at the selected potential region (\approx 1.45 to \approx 1.75 V). The Tafel slope for Co₂-NiSe/NF was the smallest, 114.55 mV dec⁻¹, indicating the fastest reaction kinetics. Further, the electrochemical impedance spectrum (EIS) was conducted at 1.53 V_{RHF} to confirm the OER kinetics. As shown in Figure 4c, all the Nyquist plots showed two semicircles, indicating there were two layers of surface exposing at the applied potential.^[19] The high-frequency semicircle was ascribed to the inner layer where the redox of catalysts themselves happened. The other semicircle at the lowerfrequency region should account for the outer layer where OER actually happened. Therefore, the Nyquist plots were fitted by the equivalent circuit illustrated in Figure 4c and the results can be found in Table S8. Generally, Co₂-NiSe/NF showed the smallest charge transfer resistance (R_{ct}) of 5.618 Ω and thus the fastest OER kinetics, consistent with the Tafel analysis.

Then, CVs at different scan rates were conducted at the non-faradic region, and the extracted double-layer capacitors (C_{dl})

and electrochemical specific area (ECSA) were calculated in Figure 4d and Figure S15 (Supporting Information). According to the results, the introduction of Co atoms would make the ECSA smaller. The calculated ECSAs of the catalysts were consistent with the SEM results that NiSe showed a nanosheet-like morphology while Co₂-NiSe/NF showed a coral-like morphology. Further, the N₂ sorption isotherms were conducted to verify the reduced specific area and pore size distribution, as shown in Figure S16 (Supporting Information). The undoped sample (Co₀-NiSe/NF) showed a higher adsorption volume and pore volume and thus a higher specific area according to the N2 sorption isotherm results. All the above characterizations agreed that the introduction of Co atoms would influence the crystalline lattice, thus influencing the morphology and surface rough factor (ECSA). Considering that the ECSA of the studied catalysts varied a lot from each other, which would lead to different amounts of active sites exposed to the reaction. Therefore, the intrinsic catalytic performance was evaluated by the ECSA normalized polarization curves, as shown in Figure 4e. Surprisingly, the intrinsic catalytic activity was in direct proportion to the relative content of R-NiSe (Figure 4f). Other catalytic performance indicators in Figure 4f also proved the increase in catalytic activity after the doping of Co and the introduction of R-NiSe. Generally, the Co₄-NiSe/NF showed the greatest intrinsic catalytic performance as evidenced by the highest ECSA normalized current density as shown in Figure 4f, which originated from the highest R-NiSe content. However, Due to the smaller ECSA compared with Co₂-NiSe/NF, the Co₄-NiSe/NF suffered from the mass transport and thus showed higher values of R_{ct} and Tafel slope. Therefore, the Co₂-NiSe/NF showed a comparable catalytic performance to that of Co₄-NiSe/NF though with a poorer intrinsic activity.

Finally, the stability of Co_2 -NiSe/NF was evaluated by chronopotentiometry (CP) at $j=10\,\mathrm{mA\,cm^{-2}}$ in 1.0 M KOH aqueous solution, as shown in Figure 4g. After 60 h of CP test, the catalytic performance showed almost no decline, with a degradation rate of only 1.2%. The result proved the great stability of the Co_2 -NiSe/NF, which might be one of the best candidates for industry application.

In summary, the introduction of Co atoms into the NiSe lattice would bring a more satisfying catalytic activity for OER. Specifically, the Co₂-NiSe/NF and Co₄-NiSe/NF would have a smaller onset potential, R_{ct}, Tafel slope and larger intrinsic activity than that of NiSe/NF. The enhancement in intrinsic activity originated from the superior electronic structure of R-NiSe. Since the Ni atoms in R-NiSe were less-coordinated than those in H-NiSe, the splitting energy of 3d orbits in R-NiSe was smaller. Consequently, the electrons would tend to occupy the $e_{\rm g}$ orbits, leading to more unoccupied states in the $t_{\rm 2g}$ orbits. As a result, additional electron transfer channels in the $t_{\rm 2g}$ orbits of R-NiSe would facilitate the electron transfer process, thus resulting in a lower overpotential and faster reaction kinetics. Moreover, the stability of Co₂-NiSe/NF was great and was promising for further applications.

2.4. The (Hybrid) Overall Water Splitting Performance

The large-scale industrial application of water splitting to generate pure hydrogen was now urgently in need of highly effective and ultra-stable multifunctional electrocatalysts. Besides, the

16136829, 0, Downloaded from https://onlinelibrary.wiley.com/doi/10.1002/smll.202305905 by National Taiwan University, Wiley Online Library on [05/12/2023]. See the Terms and Conditions (https://onlinelibrary.wiley.com/erms

and-conditions) on Wiley Online Library for rules of use; OA articles are governed by the applicable Creative Commons License

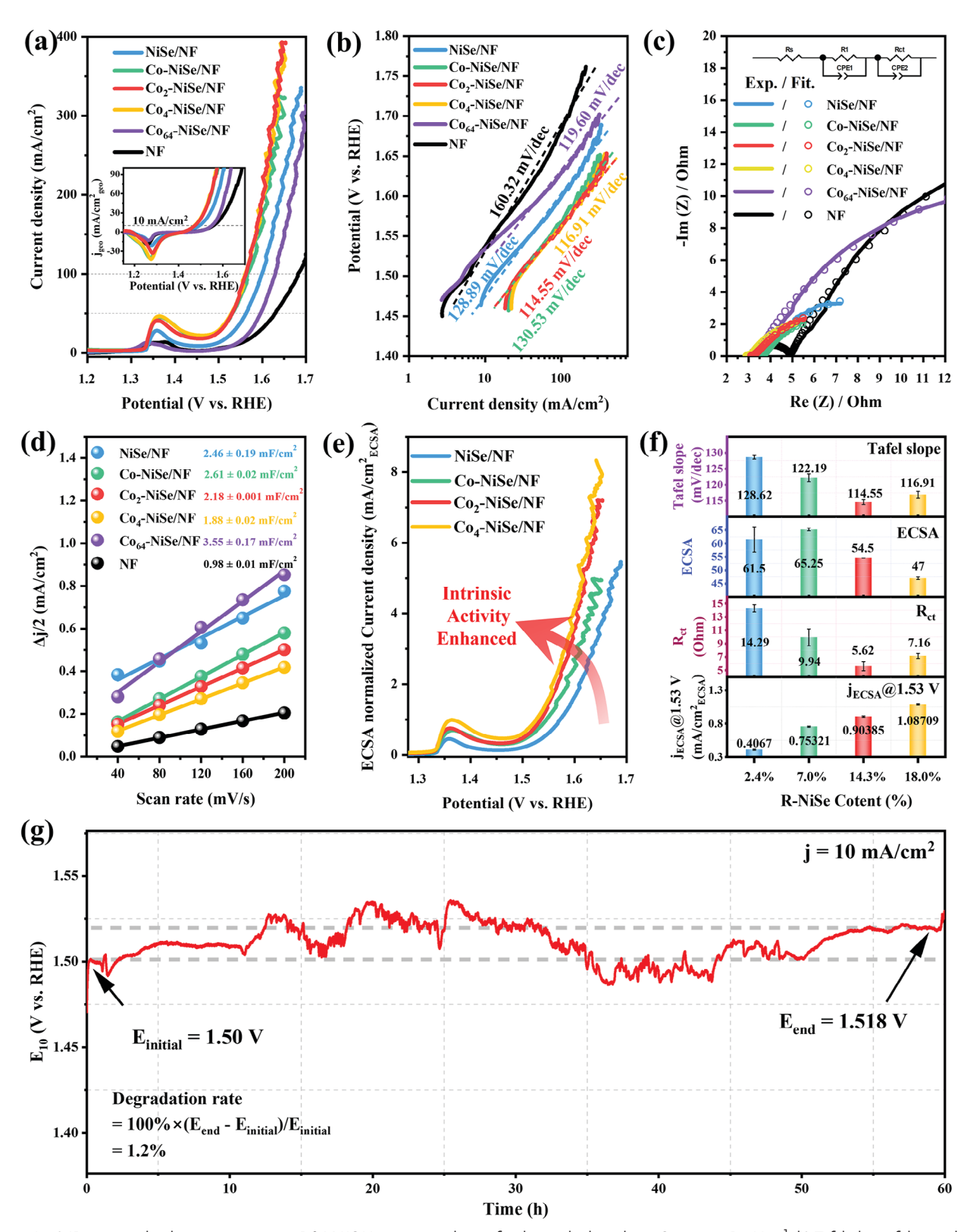


Figure 4. a) IR-corrected polarization curves in 1.0 M KOH aqueous solution for the studied catalysts. Scan rate: 1 mV s⁻¹. b) Tafel plots of the catalysts. c) The Nyquist plots of the catalysts from both experiments and fittings. d) Calculations of C_{d1} and thus ECSA according to the CVs. e) ECSA normalized polarization curves in 1.0 M KOH aqueous solution. f) Comparison of Tafel slope, ECSA, charge transfer resistance and intrinsic activity. The error bars were plotted based on the fitting errors and the diversity of repeated experiments. g) Chronopotentiometry at j = 10 mA cm⁻² for Co₂-NiSe/NF in 1.0 M KOH aqueous solution.

16136829, 0, Downloaded from https://onlinelibrary.wiley.com/doi/10.1002/smll.202305905 by National Taiwan University, Wiley Online Library on [05/12/2023]. See the Terms

and Conditions (https://onlinelibrary.wiley.com/terms

and-conditions) on Wiley Online Library for rules of use; OA articles are governed by the applicable Creative Commons License

www.small-journal.com

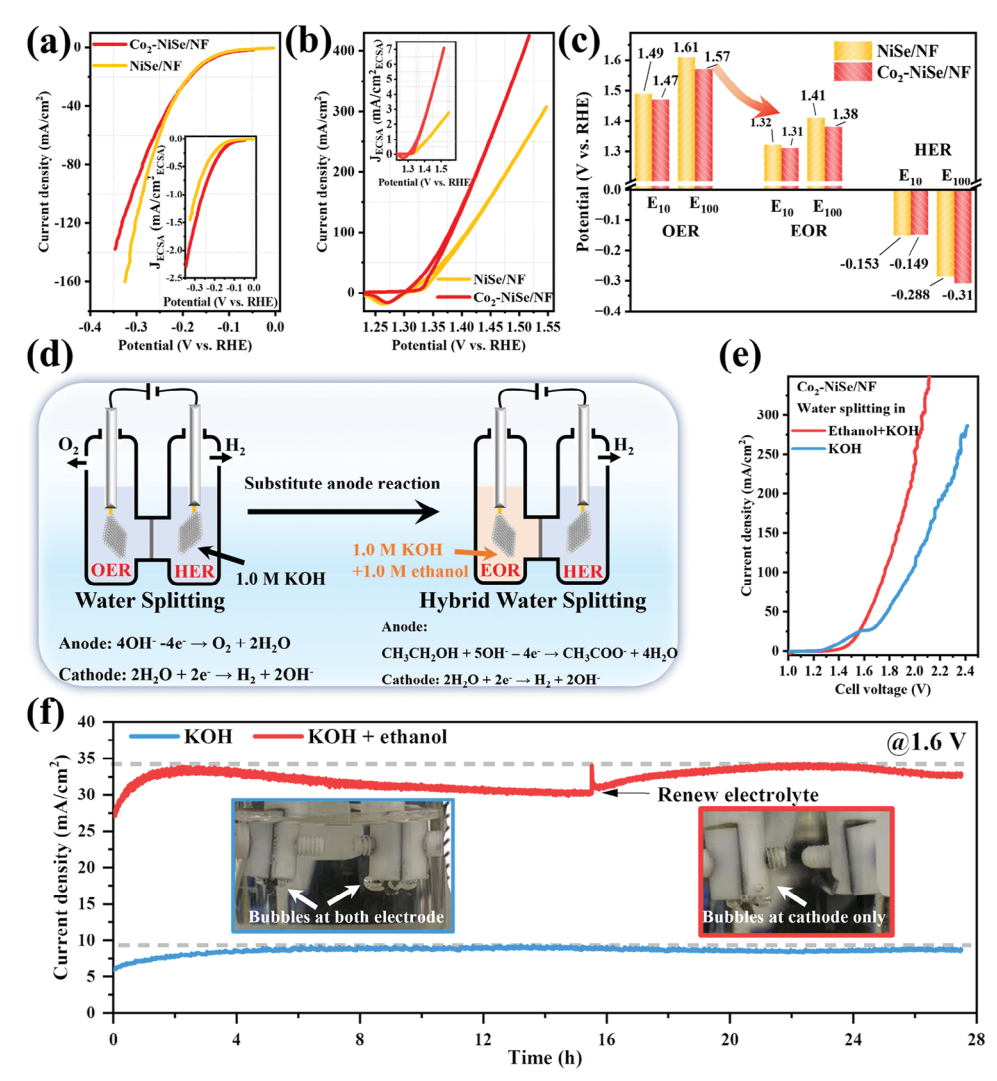


Figure 5. a) The HER polarization curves for NiSe/NF and Co_2 -NiSe/NF. b) The EOR polarization curves for NiSe/NF and Co_2 -NiSe/NF. The insets in a and b are the ECSA normalized polarization curves. c) Histogram to compare the OER, EOR and HER catalytic activity for NiSe/NF and Co_2 -NiSe/NF. d) Schematic diagram of the traditional water splitting and the hybrid water splitting devices. e) The two-electrode IR-corrected polarization curves for Co_2 -NiSe/NF in 1.0 M KOH and 1.0 M KOH containing 1.0 M ethanol. f) J-t curves at 1.6 V for Co_2 -NiSe/NF in 1.0 M KOH and 1.0 M KOH containing 1.0 M ethanol.

ethanol oxidation reaction (EOR) had a lower equilibrium potential than that of OER. ^[9] Therefore, replacing the OER at the anode of water splitting with EOR might further lower the cell voltage for water splitting.

Therefore, the HER and EOR performance of NiSe/NF and Co₂-NiSe/NF were studied as shown in **Figure 5a–c**. For HER, thanks to the faster two-electron process than that of OER, both of the catalysts showed η_{10} of ≈ 150 mV. In Figure 5a, the HER catalytic performance of NiSe/NF surpassed Co₂-NiSe/NF at the high overpotential region. This was caused by the larger ECSA and thus better mass transfer for NiSe/NF. However, after normalized by ECSA (inset in Figure 5a), one can easily see that the intrinsic HER activity of Co₂-NiSe/NF was better than that of NiSe/NF.

More interestingly, the two catalysts showed benign EOR catalytic activity, as shown in Figure 5b. Both of the studied cata-

lysts reached the current density of 10 mA cm $^{-2}$ at $\approx 1.3~V_{\rm RHE}$, which was $\approx 200~mV$ lower than their E_{10} for OER. Specifically, for Co $_2$ -NiSe/NF, the E_{10} for OER was 1.47 V and E_{10} for EOR was 1.31 V. If replacing the anode OER with EOR for water splitting, the cell voltage can reduce 160 mV, which was already a great breakthrough for overall water splitting.

Therefore, inspired by the great catalytic performance of Co₂NiSe/NF for OER, HER and EOR, overall water-splitting and hybrid water-splitting devices were set up as illustrated in Figure 5d. For both of the water-splitting devices, pure $\rm H_2$ would be generated from the cathodes. The electrolyte at the anode for traditional water splitting was 1.0 M KOH, and thus pure $\rm O_2$ would be generated from the anode for traditional water splitting devices. For hybrid water splitting devices, the electrolyte at the anode was 1.0 M KOH containing 1.0 M ethanol, and thus the anode resultants might be $\rm CO_x$ or acetate. $^{[8]}$ Then, the catalytic performances

www.advancedsciencenews.com



16136829, D. Downloaded from https://oinleibtrary.wilej.co.orn/doi/10.1002/smll.20230959 by National Tawau University, Wiley Online Library on [0512023]. Sethe te Terms and Conditions (https://onlineibtrary.wiley.com/terms-and-conditions) on Wiley Online Library or rules of use; OA articles are governed by the applicable Creative Commons License and Conditions (https://onlineibtrary.wiley.com/terms-and-conditions) on Wiley Online Library or rules of use; OA articles are governed by the applicable Creative Commons License and Conditions (https://onlineibtrary.wiley.com/terms-and-conditions) on Wiley Online Library or rules of use; OA articles are governed by the applicable Creative Commons License and Conditions (https://onlineibtrary.wiley.com/terms-and-conditions) on Wiley Online Library or rules of use; OA articles are governed by the applicable Creative Commons License and Conditions (https://onlineibtrary.wiley.com/terms-and-conditions) on Wiley Online Library or rules of use; OA articles are governed by the applicable Creative Commons License and Conditions (https://onlineibtrary.wiley.com/terms-and-conditions) on Wiley Online Library or rules of use; OA articles are governed by the applicable Creative Commons License and Conditions (https://onlineibtrary.wiley.com/terms-and-conditions) on Wiley Online Library or rules of use; OA articles are governed by the applicable Creative Commons License and Conditions (https://onlineibtrary.wiley.com/terms-and-conditions) on Wiley Online Library or rules of use; OA articles are governed by the applicable Creative Commons License and Conditions (https://onlineibtrary.wiley.com/terms-and-conditions) on Wiley Online Library or rules of use; OA articles are governed by the applicable Creative Commons License and Conditions (https://onlineibtrary.wiley.com/terms-and-conditions) on Wiley Online Library or rules of use; OA articles are governed by the applicable Creative Commons License and Conditions (https://onlineibtrary.wiley.com/terms-and-conditions) on the applicable

www.small-journal.com

of $\rm Co_2$ -NiSe/NF for both traditional and hybrid water splitting were studied as shown in Figure 5e. As expected, the hybrid water splitting showed enhanced performance for water splitting. To be specific, the overpotential for 50 and 200 mA cm $^{-2}$ decreased for 142 and 291 mV, respectively. Additionally, the stability of $\rm Co_2$ -NiSe/NF for both traditional and hybrid water splitting were satisfying as shown in Figure 5f. The catalytic performance of (hybrid) water splitting showed an enhancement during the first few hours and then remained stable for more than 20 h (Figure S17, Supporting Information).

To sum up, besides the benign OER catalytic activity, the $\rm Co_2$ -NiSe/NF also showed satisfying HER and EOR catalytic performance. Additionally, the intrinsic catalytic performance of $\rm Co_2$ -NiSe/NF for HER and EOR were better than that of NiSe/NF. Therefore, the $\rm Co_2$ -NiSe/NF also showed favorable performance for traditional and hybrid water splitting, and thus a promising candidate for further application.

2.5. The DFT Calculations

DFT calculations were conducted in order to elucidate the change in electronic structure. As can be seen in Figure 6a, the Ni-3d band structures of H-NiSe and R-NiSe were guite different. First of all, the d-band center of R-NiSe was much higher than that of H-NiSe. Prior research has proven that the upshift of the *d*-band center would facilitate the adsorption of reaction intermediates and thus alter the catalytic performance.[11,39,40] The *d*-band center was -5.7 eV for H-NiSe and -3.1 eV for R-NiSe according to Figure 6a. An upshift of 2.6 eV for the *d*-band center indicated the adsorption ability of R-NiSe was much better than that of H-NiSe. Second, the density of state (DOS) for R-NiSe was more continuous compared with that of H-NiSe, especially near the Fermi level. Specifically, the R-NiSe showed nearly zero band gap and would show a metallic characteristic with better electronic conductivity. On the contrary, the H-NiSe showed a band gap in DOS and would show a semiconductor behavior. The broader band gap for H-NiSe came from the bigger splitting energy (Δ) of the crystal field (Figure 6b). The Ni atoms in H-NiSe were six-coordinated in an octahedral field while five-coordinated in R-NiSe. The reduced coordination number means a decrease in electrostatic repulsion and thus a smaller splitting energy. In other words, electrons might prefer to occupy the e_{σ} orbits of R-NiSe because of the lower barrier as compared to H-NiSe.

Inspired by this, the orbital occupancies of Ni-3d for H-NiSe and R-NiSe were calculated as shown in Figure 6c. The average orbit filling of e_g was 1.528 for R-NiSe, while it was 1.197 for H-NiSe, which indicated the higher barrier for electrons to occupy the e_g orbits caused by the six-coordinated crystal field in H-NiSe. On the contrary, the average orbit filling of t_{2g} was 1.883 for R-NiSe while 1.949 for H-NiSe. Generally, the R-NiSe showed an increasing number of e_g occupancy and decreasing number of t_{2g} occupancy, as compared with H-NiSe. The nearly all-full occupancy of t_{2g} for H-NiSe confirmed the low spin-state electron configuration of H-NiSe. For R-NiSe, more electrons tend to occupy the e_g orbits because of the relatively lower barrier of splitting energy compared with the pairing energy, leaving more unoccupied or half-occupied states in t_{2g} orbits (Figure 6d). Since the Ni- t_{2g} orbits showed the same symmetry as the coordinated O/Se-p orbits,

the electrons can only hop between Ni-3d to O/Se-p through the unoccupied states in t_{2g} . The t_{2g} occupancy of H-NiSe was nearly all-full (1.949/2), therefore the electron hopping between Ni-3d to O/Se-p was forbidden (Figure 6d). For R-NiSe, there were more unoccupied states in t_{2g} orbits (1.883/2), and thus the electron transfer process was more favorable in R-NiSe.

Further, the electron density difference was conducted to further study the electron transfer process, as shown in Figure 6e–h. In H-NiSe, the electrons can transfer from Ni atoms to Se atoms (Figure 6e) because the electronegativity of Se is higher than that of Ni. Therefore, the Ni in H-NiSe was in a positive valent state and Se was in a negative valent state, in agreement with the XPS results. The electron transfer process in R-NiSe showed a similar trend, from Ni to Se as shown in Figure 6g. However, the Ni was more electron-deficient in R-NiSe (-0.31) compared with that of H-NiSe (-0.29). The results indicated a lower electron density of the Ni atoms and thus a higher valent state of Ni in R-NiSe compared with H-NiSe. Further, the doping of Co atoms into the lattice had a great influence on the electron transfer process of both H-NiSe and R-NiSe. As shown in Figure 6f, electrons would transfer from Co atoms to Ni atoms, increasing the electron density near the Ni atoms compared with the undoped one (from -0.29to -0.28). The electron transfer from Co to Ni is conventional due to the slightly lower electronegativity of Co (1.88) compared to Ni (1.91). Therefore, the doping of Co atoms is supposed to increase the electron density near the Ni atoms. However, in Codoped R-NiSe (Figure 6h), an unconventional electron transfer was found. To be more specific, the Ni atoms adjacent to the Co atoms showed a more pronounced decrease in electron density (-0.30) compared with the distant Ni atoms (-0.29). Accordingly, the nearby Se atoms also showed an increase in electron density compared with the distant ones (from 0.27 to 0.35). The results indicated that the electrons might transfer from Ni atoms to the nearby Co/Se atoms, resulting in a decrease in electron density near the Ni atoms of Co-doped R-NiSe. The unconventional electron transfer was another proof of the unoccupied states in the t_{2g} orbits of R-NiSe.

Inspired by the excellent electronic structure of R-NiSe, the Gibbs free energy changes of the reaction intermediates were further calculated as shown in Figure 7. According to Figure 2m, the H-NiSe(102)/R-NiSe(211) heterostructure interface was directly observed by HRTEM. Therefore, the H-NiSe(102) was used as the exposed facet for DFT calculations of H-NiSe (Figure 7a). Similarly, the H-NiSe/R-NiSe heterostructure was constructed with H-NiSe (102) and R-NiSe(211) facets (Figure 7b). Since all the catalysts were composed of more than 80% of hexagonal phase of NiSe, the reaction intermediates were adsorbed on the surface of hexagonal phase of NiSe for both H-NiSe and H-NiSe/R-NiSe (Figure 7a,b). As can be seen in Figure 7c, at U = 0 V, the free energy diagrams went uphill for the two surfaces. The two studied surfaces showed the same rate-determined step (RDS) for OER, that was, the adsorption of OH radical on *O (*O to *OOH). Accordingly, the H-NiSe/R-NiSe showed a smaller free energy change of the RDS (ΔG_{RDS}) compared with H-NiSe. The smaller the ΔG_{RDS} value, the better the catalytic performance toward OER.[41,42] Therefore, the H-NiSe/R-NiSe heterostructure would show a better catalytic performance than that of H-NiSe. Further, the HER catalytic performance was calculated by evaluating the free energy change the adsorption of H atom (ΔG_{*H}).

16136829, 0, Downloaded from https://onlinelibrary.wiley.com/doi/10.1002/smll.202305905 by National Taiwan University, Wiley Online Library on [05/12/2023]. See the Terms

conditions) on Wiley Online Library for rules of use; OA articles are governed by the applicable Creative Commons License

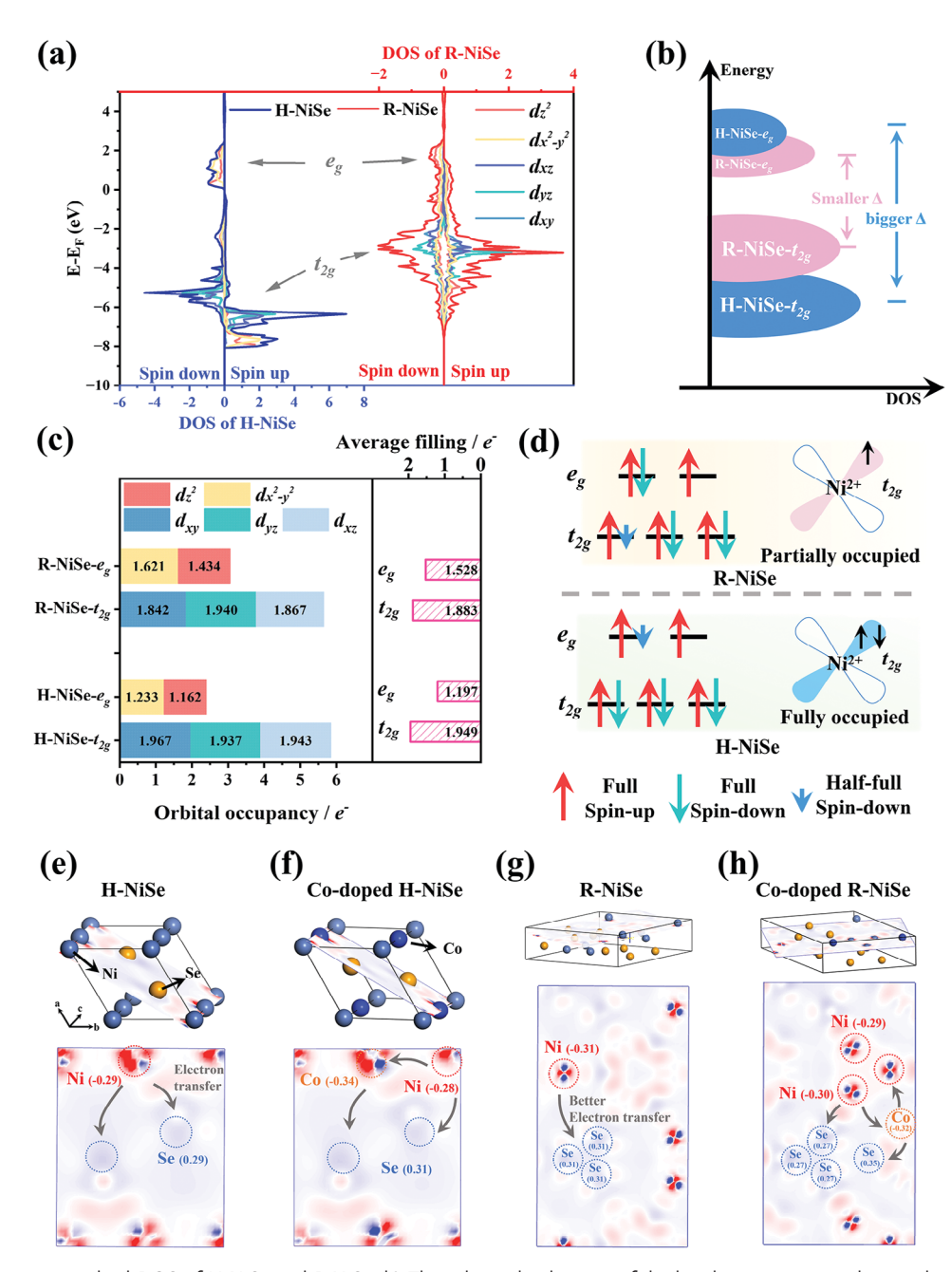


Figure 6. a) Spin-state resolved DOS of H-NiSe and R-NiSe. b) The schemadic diagram of the band structure according to the calculations. c) The calculated orbital occupancy. d) The schematic diagram of the spin state according to the DFT calculations. The ball-stick model and the corresponding electron density difference of e) H-NiSe, f) Co-doped H-NiSe, g) R-NiSe and h) Co-doped R-NiSe.

As can be seen in Figure 7d, both the ΔG_{*H} of H-NiSe and H-NiSe/R-NiSe were positive, indicating the adsorption-determined characteristic for HER, which were similar to that of OER. Specifically, the H-NiSe/R-NiSe showed a smaller ΔG_{*H} value (0.79 eV) compared with H-NiSe (1.38 eV). Thus, the H-NiSe/R-NiSe was predicted to show a better catalytic performance toward HER

To further study the potential-dependent OER performance of H-NiSe/R-NiSe and H-NiSe, the reaction coordinates were calculated at different applied potentials, as shown in Figure 7e,f.

For H-NiSe/R-NiSe, with the increasing applied potentials, the free energies for all steps were reduced while the RDS remained the same step, but the value became smaller (highlighted in green in Figure 7e). Especially for U = 1.79 V, the $\Delta G_{\rm RDS}$ became zero. The results indicated that when the applied potential surpassed 1.79 V, the OER process would become spontaneous for H-NiSe/R-NiSe. However, for H-NiSe, it needed at least 2.74 V to make all the free energy changes downhill according to Figure 7f. In other words, the OER kinetics was more favorable for H-NiSe/R-NiSe compared with H-NiSe.

16136829, 0, Downloaded from https://onlinelibrary.wiley.com/doi/10.1002/smll.202305905 by National Taiwan University, Wiley Online Library on [05/12/2023]. See the Terms and Conditions (https://onlinelibrary.wiley

conditions) on Wiley Online Library for rules of use; OA articles are governed by the applicable Creative Commons I

www.small-journal.com

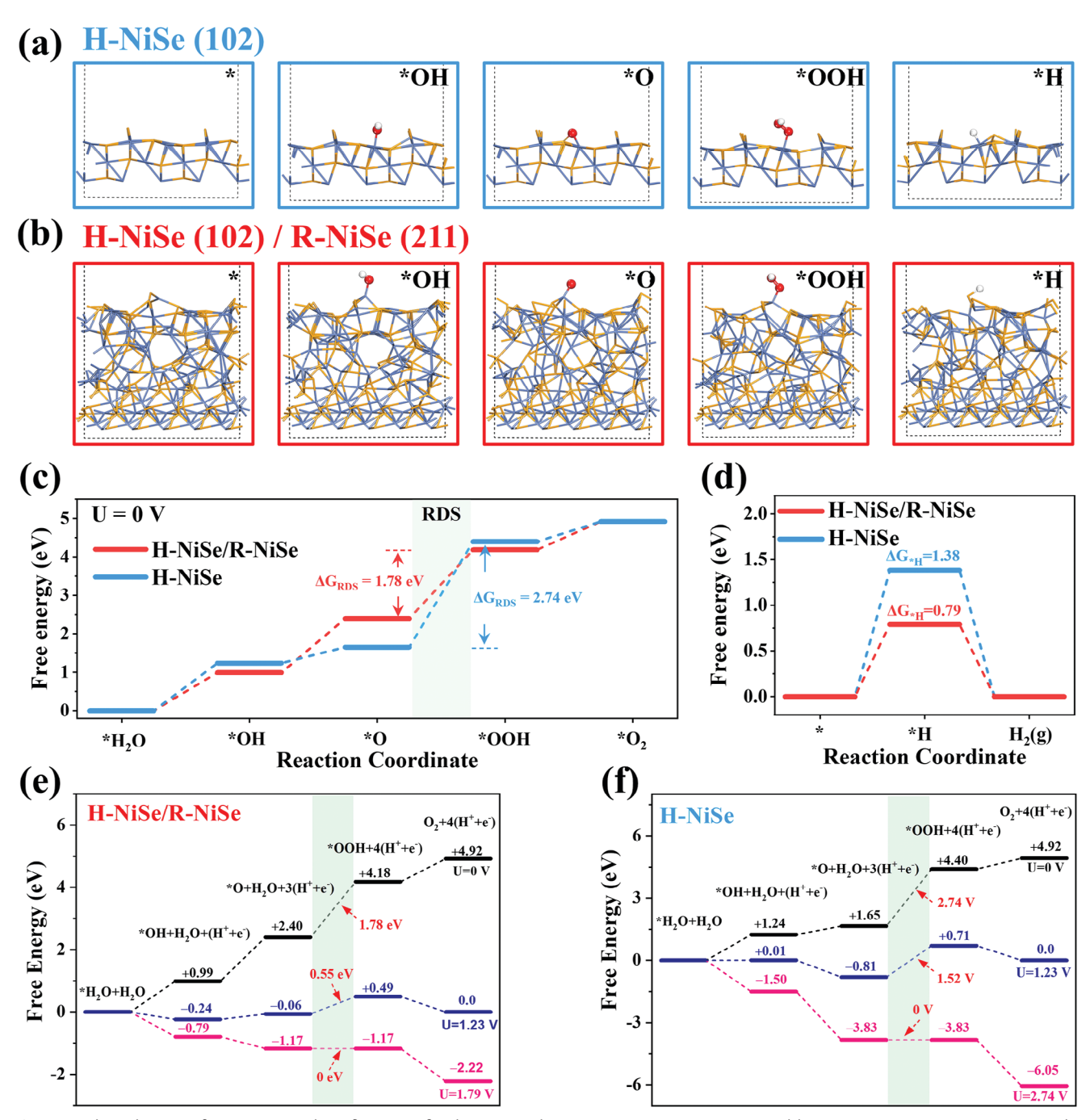


Figure 7. The side view of DFT-optimized configuration for the OER and HER process over a) H-NiSe and b) H-NiSe(102)/R-NiSe(211). Here, the asterisk (*) represented the active sites. The DFT-calculated Gibbs free energy changes of intermediate states involved in c) OER and d) HER processes for H-NiSe/R-NiSe and H-NiSe at U = 0 V. The DFT-calculated Gibbs free energy changes of intermediates states involved in OER at different applied potentials for e) H-NiSe/R-NiSe and f) H-NiSe.

To sum up, the DFT calculations proved that the *d*-band center of R-NiSe was higher than that of H-NiSe, which favored the adsorption of reaction intermediates. Additionally, the DOS was more continuous, and a metal-like behavior was found in R-NiSe. Besides, there are more unoccupied states in the $t_{2\sigma}$ orbits in R-NiSe compared with H-NiSe. The unoccupied t_{2g} orbits would then act as additional channels for electron hopping and facilitate the electron transfer process. As a result, compared with H-NiSe, the H-NiSe/R-NiSe showed a more satisfying adsorption ability for the reaction intermediates for both OER (*O to *OOH) and HER (* to *H), and thus a better catalytic performance. The results were also in good agreement with the XPS results that after the formation of R-NiSe, the general electron density near the Ni atoms decreased and the average valent state of Ni atoms

www.small-journal.com

increased. As a result, the formation of five-coordinated R-NiSe can improve the overall catalytic performance of the material.

3. Conclusion

In summary, in this work, a series of selenides named Co_x-NiSe, /NF were synthesized by adjusting the additive amount of Co (x) and Se (y). According to the XRD refinement results, trace amounts of Co doping would induce the phase transformation from six-coordinated H-NiSe to five-coordinated R-NiSe $(0 \le x \le 4)$, resulting in the formation of H-NiSe/R-NiSe heterostructure. Accordingly, the maximum content of R-NiSe was ≈18% for Co₄-NiSe/NF and further increasing the additive amount of Co wouldn't trigger additional phase transition for x > 4. The cobalt atoms existed in the lattice of NiSe as a dopant and the trigger for phase transition.

Further characterizations indicated that the formation of R-NiSe would benefit the electron transfer process by providing additional electron channels in the $t_{2\sigma}$ orbits. The R-NiSe was in a five-coordinated structure with a narrower splitting energy and thus the $t_{2\sigma}$ orbits were emptier. Consequently, the electron transfer process in H-NiSe/R-NiSe was enhanced compared with pure H-NiSe. As a result, the electrons can transfer from Ni- $t_{2\sigma}$ to Se-pand then further transfer to Co- t_{2o} , resulting in a decrease in electron density near the Ni atoms and an increasing valent state of Ni near the heterostructure.

As a result, the Co_2 -NiSe/NF with an R-NiSe content of $\approx 14\%$ showed the greatest catalytic performance toward OER, HER and EOR. For OER, the E_{10} for Co_2 -NiSe/NF was only 1.47 V_{RHE} in 1.0 M KOH solution, with an enhancement of ≈30 mV compared with the NiSe/NF and surpassed many recently reported catalysts. More impressively, the OER intrinsic catalytic activity at 1.50 V_{RHE} for Co₂-NiSe/NF was more than twice higher than that of NiSe/NF. Besides, the Co₂-NiSe/NF also showed benign HER and EOR catalytic activity, with E_{10} of -0.149 V_{RHE} for HER and 1.31 V_{RHE} for EOR and making it a trifunctional catalyst for overall water splitting. The promotion in catalytic performance was further verified by DFT calculation to be the enhancement in adsorption ability after the introduction of R-NiSe.

This work found an important and interesting interaction between the doping Co atoms and nickel selenide. The crystal structure, electronic structure and thus catalytic performance were successfully altered by a simple doping method. Further, the method was facile in terms of reaction temperature and synthesis procedure compared with many other previous literature, which might offer a new approach for future catalyst design.

4. Experimental Section

Chemicals: Selenium powder (Se, 99.9%), cobalt chloride (CoCl₂·6H₂O, 99.99%), sodium borohydride (NaBH₄, >98%) were purchased from Aladdin Ltd. of Shanghai. N, N-dimethylformamide (DMF, 99%) and potassium hydroxide (KOH, >95%) were purchased from Macklin Biochemical Ltd. of Shanghai. The nickel foam (NF, 1.5 mm in thickness) was purchased from Lige Ltd. The absolute ethanol (99.7%) was purchased from Meryer Ltd. All the water used was deionized water produced by an ultrapure water system (HITECH, 18.2 M Ω). All chemicals were used as received without further purification.

Synthesis of Co_x-NiSe_y/NF: The Co_x-NiSe_y/NF was synthesized through an one-step hydrothermal method by adjusting the additive

amount of cobalt chloride (x) and selenium powder (y). Take Co-NiSe/NF as an example (x = y = 1). First, a piece of nickel foam (NF, 2.0×2.0 cm) was pre-treated in the diluted hydrochloric acid solution (50% vol.%) for 20 min and rinsed with deionized water before use. Second, 64.0 mg of Se powder and 46.0 mg of NaBH₄ were added into 15.0 mL of DMF and stirred for 1 h to form solution A. Meanwhile, 6.0 mg of CoCl₂·6H₂O was added into another 15.0 mL DMF and stirred for 1 h to form solution B. Then, solution A and B were mixed and stirred for another 20 min. After that, the mixed solution was transferred to a 50 mL Teflon-lined autoclave with a piece of pre-treated NF. The autoclave was then sealed and heated to 160 °C for 12 h in an oven. Finally, after cooling down naturally, the Co_v-NiSe,/NF was rinsed with deionized water carefully and dried at 60 °C overnight.

Here, the x and y in Co_x -NiSe $_y$ /NF represented the additive amount of CoCl₂·6H₂O and selenium powder for hydrothermal reaction but NOT the actual stoichiometric ratio of the materials. When x = 1, the additive amount of cobalt chloride was 6.0 mg while it was 12.0 mg for x = 2. Especially when x = 0, it turned out to be the undoped NiSe_v/NF. In this case, other procedures remained the same except that there was no cobalt chloride added into solution B. Similarly, 64.0 mg and 128.0 mg of selenium powder were used as reactants for y = 1 and y = 2, respectively.

Structural Characterizations: To avoid the overlapping of XRD patterns of NF and the restrictions of TEM, the Co_x-NiSe_v powder was collected by ultrasonic concussion and cleaned with ethanol. Other characterizations were performed on Co_v-NiSe_v/NF.

XRD measurements were performed on Miniflex 600 diffractometer (Cu $K\alpha$, $\lambda = 1.54056$ Å). SEM was performed on Philips XL-30ESEM (5 kV, In-Lens) and TEM was performed on JEOL JEM-2100F (200 kV). XPS was performed on Thermo Fisher Scientific ESCALAB250 (Al K α , h ν = 1486.6 eV). Raman spectrums were collected on HORIBA LabRAM HR Evolution with an excitation source of 633 nm or Zolix RTS-mini with a continuous laser of 532 nm

Electrochemical Characterizations: The catalytic performance for OER, HER and EOR were studied in a typical three-electrode system with a graphite rod as the counter electrode and a Hg/HgO electrode as the reference electrode, respectively. The Co_x-NiSe_v/NF was first cut into $0.5~\text{cm} \times 0.5~\text{cm}$ in size and then embedded into an electrode holder to act as the working electrode. The electrolyte was 1.0 M KOH for OER/HER and 1.0 M KOH containing 1.0 M ethanol for EOR. All the electrochemical data were collected with electrochemical workstations (CHI660E or BioLogic-VSP-300). All the potentials had been converted into potentials against reversible hydrogen electrode (RHE) if not especially stated. Linear sweep voltammetry (LSV) curves were collected at a scan rate of 5 mV s⁻¹ for HER and EOR and 1 mV s⁻¹ for OER. Electrochemical impedance spectroscopy (EIS) measurements were performed at 1.53 V_{RHE} and fitted with an EIS fitting software (Zview, version 2.9c). Electrochemical specific surface area (ECSA) was evaluated by the double-layer capacitor (C_{dl}). Specifically, open-circuit potentials were first measured for each material to find the non-faradic regions. Then, CVs with scan rates of 20–200 mV s⁻¹ were performed between the non-faradic region. Subsequently, C_{dl} and ECSA were calculated by:

$$C_{\rm dl} = \frac{1}{2} \frac{\Delta j}{\Delta R}, ECSA = \frac{C_{\rm dl}}{C_{\rm S}} \tag{1}$$

Here, j was the current density of CVs at a specific potential and Rwas the scan rate. Then, $\frac{\Delta j}{\Delta R}$ was the slope of the *j-R* curve. C_s was the double-layer capacitor value for an ideal smooth ball and the value was $0.04~\text{mF/cm}^{-2}$ according to the previous literature. [43]

DFT Calculations: Density functional theory (DFT) calculations were performed using the open-source plane-wave code, Quantum Espresso, with the generalized gradient approximation and the projector augments wave pseudopotentials by the Perdew-Burke-Ernzerhof function for exchange-correlation energy. The k-point and plane-wave cutoff energy were set to "fine". The atomic positions were relaxed until the force on each atom was under 0.03 eV \mathring{A}^{-1} and the convergence tolerance of the energy was set to 10⁻⁵ eV. To avoid interplanar interactions, the vacuum

16136829, 0, Downloaded from https://onlinelibrary.wiley.com/doi/10.1002/smll.202305905 by National Taiwan University, Wiley Online Library on [05/12/2023]. See the Terms and Conditions (https://onlinelibrary.wiley.com/ems

and-conditions) on Wiley Online Library for rules of use; OA articles are governed by the applicable Creative Commons License

www.small-journal.com

space was more than 10 Å. The unit cell of H-NiSe was in the P63/mmc group, and R-NiSe was in the R3m group. For geometry optimization of all slab models, the top layers were allowed to relax. The Gibbs free energy difference (ΔG_0) was 4.92 eV for the OER reaction at p=1 bar and T=298.15 K. The reaction was generally believed to proceed in four steps:

$$H_2O(I) + * \rightarrow OH* + (H^+ + e^-)$$
 (2)

$$OH* \rightarrow O* + (H^+ + e^-) \tag{3}$$

$$H_2O(I) + O* \rightarrow OOH* + (H^+ + e^-)$$
 (4)

$$OOH* \rightarrow O_2 + (H^+ + e^-) + *$$
 (5)

where * represents the active site of the catalyst, and OOH*, O*, and OH* represent the species adsorbed on the active site. At the standard condition (p = 1 bar and T = 298.15), the Gibbs free energy of $H^+ + e^-$ equals the Gibbs free energy of $1/2 H_2$.

Supporting Information

Supporting Information is available from the Wiley Online Library or from the author.

Acknowledgements

J.X. and J.R. contributed equally to this work. This work was supported by the National Natural Science Foundation of China (61988102, 22075102, 22005120, 21576301, 51973244, 12174154, 21703081 and 22209056), the Key Research and Development Program of Guangdong Province (2019B090917007), the Science and Technology Planning Project of Guangdong Province (2019B090909011), the Natural Science Foundation of Guangdong Province, China (2021A1515010090), the Guangdong Basic and Applied Basic Research Foundation (2023A1515010921, 2023A1515010270), the Fundamental Research Funds for the Central Universities (21619317 and 21620329), the Postdoctoral Research Foundation of China (2020M673071), and the Science and Technology Planning Project of Guangzhou, China (Grant No. 201605030008, 202102020963, 202201010125).

Conflict of Interest

The authors declare no conflict of interest.

Data Availability Statement

The data that support the findings of this study are available from the corresponding author upon reasonable request.

Keywords

electronic structure, non-precious metal electrocatalysts, overall water splitting, phase transition

> Received: July 13, 2023 Revised: October 12, 2023 Published online:

- [1] D. A. Kuznetsov, B. Han, Y. Yu, R. R. Rao, J. Hwang, Y. Román-Leshkov, Y. Shao-Horn, Joule 2018, 2, 225.
- [2] J. Song, C. Wei, Z.-F. Huang, C. Liu, L. Zeng, X. Wang, Z. J. Xu, Chem. Soc. Rev. 2020, 49, 2196.
- [3] J. T. Mefford, A. R. Akbashev, M. Kang, C. L. Bentley, W. E. Gent, H. D. Deng, D. H. Alsem, Y.-S. Yu, N. J. Salmon, D. A. Shapiro, P. R. Unwin, W. C. Chueh, Nature 2021, 593, 67.
- [4] J. Suntivich, K. J. May, H. A. Gasteiger, J. B. Goodenough, Y. Shao-Horn, Science 2011, 334, 1383.
- [5] X. Wang, S. Xi, P. Huang, Y. Du, H. Zhong, Q. Wang, A. Borgna, Y.-W. Zhang, Z. Wang, H. Wang, Z. G. Yu, W. S. V. Lee, J. Xue, Nature 2022, 611, 702.
- [6] X.-L. Zhang, S.-J. Hu, Y.-R. Zheng, R. Wu, F.-Y. Gao, P.-P. Yang, Z.-Z. Niu, C. Gu, X. Yu, X.-S. Zheng, C. Ma, X. Zheng, J.-F. Zhu, M.-R. Gao, S.-H. Yu, Nat. Commun. 2019, 10, 5338.
- [7] S. Li, R. Ma, J. Hu, Z. Li, L. Liu, X. Wang, Y. Lu, G. E. Sterbinsky, S. Liu, L. Zheng, J. Liu, D. Liu, J. Wang, Nat. Commun. 2022, 13, 2916.
- [8] Z. Li, S. Ning, J. Xu, J. Zhu, Z. Yuan, Y. Wu, J. Chen, F. Xie, Y. Jin, N. Wang, H. Meng, S. Sun, Energy Environ. Sci. 2022, 15, 5300.
- [9] J. Xu, B.-X. Wang, D. Lyu, T. Wang, Z. Wang, Int. J. Hydrogen Energy **2023**, 48, 10724.
- [10] D. Y. Chung, P. P. Lopes, P. Farinazzo Bergamo Dias Martins, H. He, T. Kawaguchi, P. Zapol, H. You, D. Tripkovic, D. Strmcnik, Y. Zhu, S. Seifert, S. Lee, V. R. Stamenkovic, N. M. Markovic, Nat Energy 2020,
- [11] I. C. Man, H.-Y. Su, F. Calle-Vallejo, H. A. Hansen, J. I. Martínez, N. G. Inoglu, J. Kitchin, T. F. Jaramillo, J. K. Nørskov, J. Rossmeisl, Chem-CatChem 2011, 3, 1159.
- [12] P. M. Bodhankar, P. B. Sarawade, G. Singh, A. Vinu, D. S. Dhawale, J. Mater. Chem. A 2021, 9, 3180.
- [13] Y. Sun, S. Sun, H. Yang, S. Xi, J. Gracia, Z. J. Xu, Adv. Mater. 2020, 32, 2003297.
- [14] Y. Liu, H. Cheng, M. Lyu, S. Fan, Q. Liu, W. Zhang, Y. Zhi, C. Wang, C. Xiao, S. Wei, B. Ye, Y. Xie, J. Am. Chem. Soc. 2014, 136, 15670.
- [15] L. Zhai, T. W. Benedict Lo, Z.-L. Xu, J. Potter, J. Mo, X. Guo, C. C. Tang, S. C. Edman Tsang, S. P. Lau, ACS Energy Lett. 2020, 5, 2483.
- [16] J. Dai, D. Zhao, W. Sun, X. Zhu, L.-J. Ma, Z. Wu, C. Yang, Z. Cui, L. Li, S. Chen, ACS Catal. 2019, 9, 10761.
- [17] Y.-R. Zheng, P. Wu, M.-R. Gao, X.-L. Zhang, F.-Y. Gao, H.-X. Ju, R. Wu, Q. Gao, R. You, W.-X. Huang, S.-J. Liu, S.-W. Hu, J. Zhu, Z. Li, S.-H. Yu, Nat. Commun. 2018, 9, 2533.
- [18] X. Wang, S. Xi, W. S. V. Lee, P. Huang, P. Cui, L. Zhao, W. Hao, X. Zhao, Z. Wang, H. Wu, H. Wang, C. Diao, A. Borgna, Y. Du, Z. G. Yu, S. Pennycook, J. Xue, Nat. Commun. 2020, 11, 4647.
- [19] W. Chen, C. Xie, Y. Wang, Y. Zou, C.-L. Dong, Y.-C. Huang, Z. Xiao, Z. Wei, S. Du, C. Chen, B. Zhou, J. Ma, S. Wang, Chem 2020, 6, 2974.
- [20] S. S. Jeon, P. W. Kang, M. Klingenhof, H. Lee, F. Dionigi, P. Strasser, ACS Catal. 2023, 13, 1186.
- [21] B. Tian, H. Shin, S. Liu, M. Fei, Z. Mu, C. Liu, Y. Pan, Y. Sun, W. A. Goddard, M. Ding, Angew Chem Int Ed 2021, 60, 16448.
- [22] X. Wang, Y. Tuo, Y. Zhou, D. Wang, S. Wang, J. Zhang, Chem. Eng. J. 2021, 403, 126297.
- [23] Z. He, J. Zhang, Z. Gong, H. Lei, D. Zhou, N. Zhang, W. Mai, S. Zhao, Y. Chen, Nat. Commun. 2022, 13, 2191.
- [24] H. Zhang, L. Wu, R. Feng, S. Wang, C.-S. Hsu, Y. Ni, A. Ahmad, C. Zhang, H. Wu, H.-M. Chen, W. Zhang, Y. Li, P. Liu, F. Song, ACS Catal. 2023, 13, 6000.
- [25] M. Yu, E. Budiyanto, H. Tüysüz, Angew Chem Int Ed 2022, 61, e202103824.
- [26] X. Zhang, Y.-Y. Zhang, Y. Zhang, W.-J. Jiang, Q.-H. Zhang, Y.-G. Yang, L. Gu, J.-S. Hu, L.-J. Wan, Small Methods 2019, 3, 1800317.
- [27] T. Ling, D.-Y. Yan, H. Wang, Y. Jiao, Z. Hu, Y. Zheng, L. Zheng, J. Mao, H. Liu, X.-W. Du, M. Jaroniec, S.-Z. Qiao, Nat. Commun. 2017, 8,

www.small-journal.com

16136829, 0, Downloaded from https://onlinelibrary.wiley.com/doi/10.1002/smll.202305905 by National Taiwan University, Wiley Online Library on [05/12/2023]. See

the Terms

and Conditions

and-conditions) on Wiley Online Library for rules of use; OA articles

are governed by the applicable Creative Commons License

- [28] Z. Zhao, H. Wu, H. He, X. Xu, Y. Jin, J. Mater. Chem. A 2015, 3, 7179.
- [29] J.-Y. Xue, F.-L. Li, B. Chen, H. Geng, W. Zhang, W.-Y. Xu, H. Gu, P. Braunstein, J.-P. Lang, Appl. Catal. B 2022, 312, 121434.
- [30] X.-L. Zhang, S.-J. Hu, Y.-R. Zheng, R. Wu, F.-Y. Gao, P.-P. Yang, Z.-Z. Niu, C. Gu, X. Yu, X.-S. Zheng, C. Ma, X. Zheng, J.-F. Zhu, M.-R. Gao, S.-H. Yu, Nat. Commun. 2019, 10, 5338.
- [31] N. S. Mcintyre, D. D. Johnston, L. L. Coatsworth, R. D. Davidson, J. R. Brown, Sur Interface Anal 1990, 15, 265.
- [32] Z. Zhou, X. Pan, L. Sun, Y. Xie, J. Zheng, L. Li, G. Zhao, Angew Chem Int Ed 2023, 62, e202216347.
- [33] A. I. Carim, F. H. Saadi, M. P. Soriaga, N. S. Lewis, J. Mater. Chem. A **2014**, 2, 13835.
- [34] B. Tian, H. Shin, S. Liu, M. Fei, Z. Mu, C. Liu, Y. Pan, Y. Sun, W. A. Goddard, M. Ding, Angew Chem Int Ed 2021, 60, 16448.
- [35] Y. Tian, X. Xue, Y. Gu, Z. Yang, G. Hong, C. Wang, Nanoscale 2020, 12, 23125.

- [36] M. Görlin, J. Ferreira De Araújo, H. Schmies, D. Bernsmeier, S. Dresp, M. Gliech, Z. Jusys, P. Chernev, R. Kraehnert, H. Dau, P. Strasser, J. Am. Chem. Soc. 2017, 139, 2070.
- [37] J. M. P. Martirez, E. A. Carter, ACS Catal. 2020, 10, 2720.
- [38] O. Van Der Heijden, S. Park, J. J. J. Eggebeen, M. T. M. Koper, Angew Chem Int Ed 2023, 62, e202216477.
- [39] J. Li, J. Song, B.-Y. Huang, G. Liang, W. Liang, G. Huang, Y. Qi Jin, H. Zhang, F. Xie, J. Chen, N. Wang, Y. Jin, X.-B. Li, H. Meng, J. Catal. 2020, 389, 375.
- [40] D. Yan, C. Xia, W. Zhang, Q. Hu, C. He, B. Y. Xia, S. Wang, Adv. Energy Mater. 2022, 12, 2202317.
- [41] L.-M. Cao, C.-G. Hu, H.-H. Li, H.-B. Huang, L.-W. Ding, J. Zhang, J.-X. Wu, Z.-Y. Du, C.-T. He, X.-M. Chen, J. Am. Chem. Soc. 2023, 145, 1144.
- [42] Y. Yang, Q.-N. Yang, Y.-B. Yang, P.-F. Guo, W.-X. Feng, Y. Jia, K. Wang, W.-T. Wang, Z.-H. He, Z.-T. Liu, ACS Catal. 2023, 13, 2771.
- [43] X. Qiao, H. Kang, Y. Li, K. Cui, X. Jia, H. Liu, W. Qin, M. Pupucevski, G. Wu, ACS Appl. Mater. Interfaces 2020, 12, 36208.